A compact scintillator-based detector for high energy neutron spectrometry

Andy Buffler, Tanya Hutton, Erin Jarvie, Richard Babut

Radiation Physics and Chemistry 220 (2024) 111698

Contents lists available at ScienceDirect

Radiation Physics and Chemistry

journal homepage: www.elsevier.com/locate/radphyschem

A compact scintillator-based detector for high energy neutron spectrometry

Andy Buffler [a,*], Tanya Hutton [a], Erin Jarvie [a], Richard Babut [b]

[a] Metrological and Applied Sciences University Research Unit (MeASURe), Department of Physics, University of Cape Town, Rondebosch, 7700, South Africa
[b] L'Institut de Radioprotection et de Sûreté Nucléaire, Cadarache, 92260, France

ARTICLE INFO

Keywords:
Compact neutron spectrometer
PSD plastic scintillator
Silicon photomultiplier

ABSTRACT

A compact neutron spectrometer consisting of a 6 mm × 6 mm × 120 mm prism of EJ-276 plastic scintillator capable of pulse shape discrimination coupled to a single silicon photomultiplier is described. In principle this device will be capable of spectroscopic measurements exceeding 100 MeV using unfolding analyses with detector response functions measured at neutron time-of-flight facilities. A characterisation of the device is described and illustrated with measurements of the detector response made at three fast neutron facilities with energies between 5.0 MeV and 63.5 MeV. Nearly mono-energetic detector response functions were used to produce neutron energy spectra by unfolding light output distributions measured with the detector in the energy range of interest.

1. Introduction

Active measurement of the energy spectrum of high energy neutrons is of topical interest in many workplace contexts such as aviation (Bartlett, 2004), space missions (Heilbronn et al., 2015; Zeitlin et al., 2023), in and around accelerator centres (Boscolo et al., 2020), and in radiation therapy (Brenner and Hall, 2008). Cosmic rays, in particular, can produce neutrons with energies extending to several GeV, posing significant risk to both people and electronic systems. For example, at an altitude of 11 km in the atmosphere of the earth, neutrons contribute up to 40% of the equivalent dose (Goldhagen et al., 2004), with peaks in the energy spectrum around 1 MeV and 100 MeV. Furthermore, during unpredictable and short-lived space weather events, the flux of solar energetic particles, and hence secondary neutrons, increases dramatically, which strengthens the case for continuous monitoring of secondary neutrons produced in both the aviation and space environments. Direct in-situ measurement of these neutron fields is challenging in these contexts due to strict restrictions on the form factor of the measurement device, including material type, weight, and power.

Detectors based on organic scintillation materials are well established (Brooks, 1979) and have benefited from a number of recent developments, and thus remain strong candidates for these applications. Liquid organic scintillators such as BC-501A or EJ-301 remain popular choices when good quality pulse shape discrimination (PSD) is required to separate events associated with neutrons and gamma rays, but are regarded as hazardous for use in many contexts, especially when coupled to high voltage photomultipliers. However, three technologies can now be combined to produce scintillation-based neutron detectors suitable for use in non-laboratory environments. Solid ("plastic") scintillator which exhibits PSD capability (Zaitseva et al., 2018), such as the EJ-276 scintillator used in the present work, removes the toxic and fire hazards associated with most liquid scintillators. Furthermore, plastic scintillators have no need for an optical window when coupled to a photodetector, and may be fairly easily produced in any geometrical form. Secondly, silicon photomultipliers (SiPMs) offer a compact alternative to traditional photomultiplier tubes and removes the requirement of high voltage. Finally, digital data acquisition and processing systems allows pulse shape discrimination to be implemented and dynamically optimised in software across a wide energy range, or implemented on specialised hardware.

We are well advanced in developing a range of different compact neutron spectrometers (Buffler et al., 2015, 2016, 2023) based on EJ-276 scintillator, SiPMs and an FPGA-based digital acquisition system. In out-of-laboratory contexts where neutron time-of-flight is not available for spectrometry, the neutron energy spectrum may be determined though methods of spectrum unfolding. The neutron energy distribution is deconvolved from the measured neutron light output spectrum using a known detector response matrix coupled with an unfolding algorithm. For organic scintillators, the detector response matrix is typically comprised of a series of normalised light output spectra for mono-energetic neutrons incident on the detector. For neutron energies below 20 MeV these response functions may be reliably simulated (Cecconello, 2019; Dietze and Klein, 1982), however at higher energies the range of the recoil particles and the increase in

* Corresponding author.
E-mail address: andy.buffler@uct.ac.za (A. Buffler).

https://doi.org/10.1016/j.radphyschem.2024.111698
Received 2 November 2023; Received in revised form 9 March 2024; Accepted 17 March 2024
Available online 18 March 2024

Fig. 1. The compact spectrometer. A 6 mm × 6 mm × 120 mm prism of EJ-276 scintillator is encased in an aluminium tube and coupled to a single SiPM housed in a 3D-printed casing.

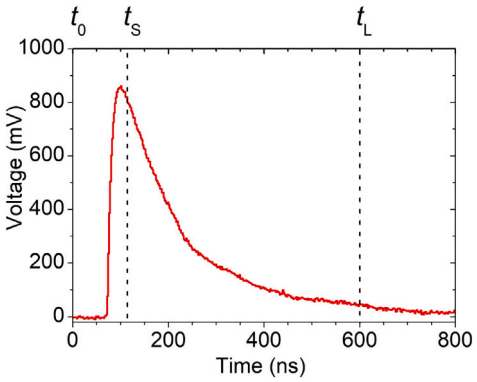

Fig. 2. A typical digitised pulse with the short t_S and long t_L integration times indicated.

available n-C reaction channels result in unreliable response functions derived from calculation (Nolte and Thomas, 2011). As the quality of the unfolded neutron energy spectrum is entirely dependent on the quality of the detector response functions, any spectral measurements above 20 MeV require measured response functions.

We present and discuss a device consisting of a prism of EJ-276 coupled to a single SiPM, and illustrate its suitability for spectrometry for high energy neutrons. Measurements of the response of the detector to quasi-monoenergetic neutrons over the energy range of interest are made via time-of-flight using a cyclotron beam, and are used to produce neutron energy spectra by unfolding light output distributions measured with the detector.

2. Methods

2.1. The detector system

Fig. 1 shows a photograph of the compact detector based on EJ-276 plastic scintillator (Eljen Technology, 2023) by Eljen Technologies and a single MicroFC-60035 silicon photomultiplier (SiPM) (onsemi, 2023) from onsemi (formerly SensL). The scintillator EJ-276 is capable of discriminating neutron events from gamma rays through pulse shape discrimination, is non-toxic, robust, can be customised in shape and size, and has been characterised over a wide range of neutron energies (Comrie et al., 2015; Ngo et al., 2023; Ryabeva et al., 2021). The MicroFC-60035 SiPM has an active area of 6 mm × 6 mm consisting of 18980 microcells, each with dimensions 35 μm × 35 μm, and was mounted on the standard SMA biasing board which features three ports: the voltage input, fast output and slow output.

The cross-sectional profile of the EJ-276 scintillator was chosen to be 6 mm × 6 mm to match the active area of the SiPM, with a length of 120 mm to be suitable for the detection of neutrons of energy exceeding 100 MeV. The scintillator was wrapped in a diffuse reflector and coupled to the single SiPM using EJ-550 optical grade silicone grease, with a specular reflecting material (3M ESR, 2023) on the opposing end. The components were housed in a light tight covering consisting of an aluminium tube covering the scintillator with a 3D-printed casing containing the SiPM (see Fig. 1). The breakdown voltage for this SiPM is approximately +24.5 V and for optimum performance an operating bias of +28.5 V (overvoltage of 16%) was used (Comrie, 2016).

The pulses from the slow output of the SiPM evaluation board were acquired in listmode with a CAEN DT5730 desktop digitiser (CAEN, 2023) and the custom open-source acquisition software QtDAQ (Comrie, 2023) via a USB-2.0 connection to a laptop. The DT5730 is an 8-channel, 14-bit digitiser with a sampling rate of 500 MS/s and features a Programmable Gain Amplifier (PGA) which allows for a voltage range of either 0.5 V_{pp} or 2.0 V_{pp}. In the present work the analysis of the acquired digitised pulses was performed post-acquisition using a series of custom-built Python scripts.

2.2. Digital pulse processing

The DT5730 unit is triggered when the absolute voltage exceeds a pre-set threshold and acquires the digitised pulse within a fixed acquisition window, an example of which is shown in Fig. 2. To account for variations in baseline voltage, the mean baseline, calculated from the 200 samples preceding the sharp change in voltage, was subtracted from each digitised pulse. In addition, since the triggering mechanism of the digitiser results in pulses that are not consistently aligned in time, a digital constant fraction discriminator (CFD) filter was applied (Comrie et al., 2015) after baseline subtraction. Assuming linear interpolation between samples, the time of zero crossing t_{cfd} for the CFD filtered pulse can be found by taking the weighted average of the samples on either side of the line of zero voltage. The start time t_0 of the pulse is defined relative to t_{cfd} as $t_0 = t_{cfd} - 150$ ns in the present work. Short and long pulse integration times, t_S and t_L respectively, were then defined relative to t_0.

The long integral parameter Q_L is a measure of the charge in the digitised pulse and is determined by integrating the digitised pulse between t_0 and t_L as shown in Fig. 2. Measurements of the Compton edges associated with the gamma ray emissions from ^{137}Cs, ^{22}Na and ^{54}Mn radioisotopic sources (see Fig. 3(a)) were used for scaling Q_L to a calibrated light output parameter L (Sole et al., 2022). The relationship between Q_L and L was found to be linear over the energy range of the gamma ray calibration sources used in the present work (Fig. 3(b)). The light output L for gamma rays may thus be expressed in MeV, and by convention the linear scale for the light output spectra measured for neutron events is denoted as MeV electron equivalent (MeV_{ee}) on the same scale. The MeV_{ee} scale may be regarded as linear above the lower L threshold of 0.25 MeV_{ee} used in the present work.

Each pulse was also integrated over a shorter time integral t_S and a pulse shape parameter S is then derived from the ratio of the long Q_L and short Q_S integrals (Comrie et al., 2015) using

$$S = k\frac{Q_S}{Q_L} + c \tag{1}$$

(with $k = 10$ and $c = 0$ for these data), which is the basis of the widely used charge comparison method of pulse shape discrimination. Signals arising from gamma ray interactions in the detector have a reduced slow decay component in comparison to those arising from neutron interactions. Therefore, a larger proportion of light output occurs within the shorter time interval for events induced by gamma rays (recoiling electrons), leading to higher values of S when compared to neutron-induced events (recoiling protons, deuterons, and alpha particles) of a similar light output. Fig. 4 shows an example of a standard L-S plot produced from the measurement made with the detector for neutrons and gamma rays produced by an ^{241}Am-^{9}Be (AmBe) source. Loci corresponding to recoiling electrons and protons

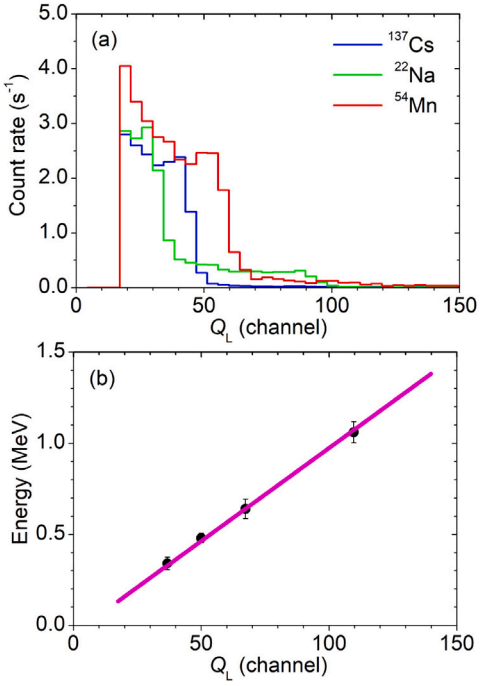

Fig. 3. (a) Uncalibrated long integral Q_L spectra for measurements of the gamma ray emissions from ^{137}Cs, ^{22}Na and ^{54}Mn; and (b) weighted linear fit of energy as a function of the Q_L values associated with the Compton edges of the distributions, with a gradient of 0.0981(9) MeV channel^{-1} and intercept of −0.01(4) MeV.

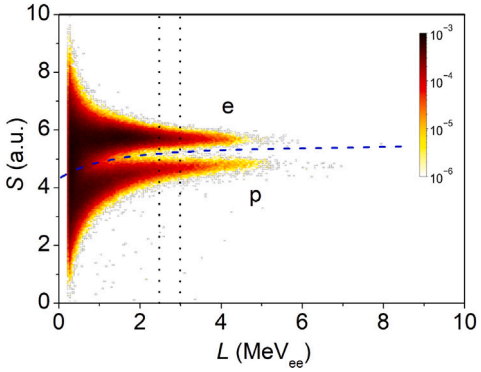

Fig. 4. Event density, normalised by the total number of measured events, as a function of light output parameter L and pulse shape parameter S for events in the detector when irradiated by the neutron and gamma ray field produced by an ^{241}Am-^{9}Be radioisotopic source. Loci associated with recoiling electrons (e) and protons (p) are identified and separated by the blue dashed curve. The vertical dotted lines select the events illustrated in Fig. 5.

are clearly distinguishable and may be separated for analysis using a cut shown by the dashed line in Fig. 4.

A Figure-of-Merit (FoM) is a useful means to provide a quantitative measurement of the separation between the distributions of S for two pulse classes associated with recoiling electrons and protons (Comrie et al., 2015). If these distributions are Gaussian in form, then it is reasonable to define a FoM in terms of the mean (μ) and full width at half maximum (FWHM) of the two distributions (see Fig. 5) by

$$\mathrm{FoM} = \frac{|\mu_e - \mu_p|}{\mathrm{FWHM}_e + \mathrm{FWHM}_p}. \quad (2)$$

The data in Fig. 5 were selected by the cut (L = 2.5 MeV$_{ee}$ to 3.0 MeV$_{ee}$) illustrated by the vertical dotted lines in Fig. 4.

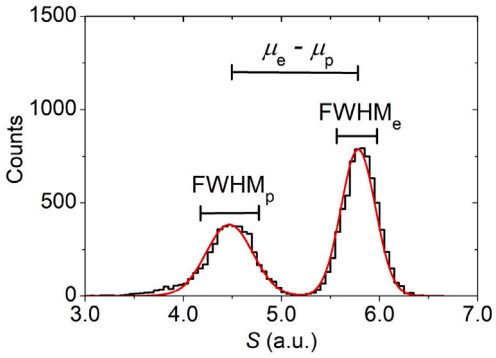

Fig. 5. The distribution of pulse shape parameter S for events with 2.5 < L < 3.0 MeV$_{ee}$ (cut shown in Fig. 4). Two Gaussian distributions have been fitted to the data. The full width half maxima of the electron (FWHM$_e$) and proton (FWHM$_e$) event distributions are indicated together with the difference between the mean values μ of the two distributions.

The short and long integration times were optimised using a FoM calculated from measurements with an AmBe source. The process requires one of the integration times to be kept constant while the other is varied. In the optimisation of the long gate the variation of the long integration time results in a variation in the relationship between Q_L and L. To ensure that the FoM was calculated with events of equivalent L the lower and upper thresholds of the selection window were chosen to be positioned relative to the Compton edge associated with the 4.4 MeV gamma ray emission from the AmBe source. The long integration time was initially set at $t_L = t_0 + 840$ ns, based on the relative pulse duration, and the short integration time was varied to produce the FoM data shown in Fig. 6(a). The optimum short integration time t_S of 120 ns was then fixed while the long integration time was varied (see Fig. 6(b)), leading to an optimised value of t_L of 600 ns. Fig. 7 shows the FoM over the full range of light output L using the optimised values of t_S and t_L, which compares favourably with measurements made with more conventional detectors (Comrie et al., 2015).

3. Measurements with fast neutron beams

The detector was characterised with measurements at three fast neutron facilities. Mono-energetic neutron beams were provided at the n-lab (Hutton and Buffler, 2024) at the University of Cape Town, South Africa, and the Accelerator for Metrology and Neutron Applications for External Dosimetry (AMANDE) facility (Gressier et al., 2004; Sole et al., 2022) of the L'Institut de Radioprotection et de Sûreté Nucléaire (IRSN), France. At the n-lab neutrons of energy 14.1 MeV are provided from a D-T sealed tube neutron generator, which is housed in a vault constructed from high density polyethylene, and a beam is shaped by a circular collimator of diameter 0.8 cm. The AMANDE facility features a 2 MV HVEE Tandetron (Gressier et al., 2014) and can produce nearly mono-energetic neutron fields using either a proton or deuteron beam directed on a target of either deuterium or tritium doped titanium. Measurements were made for neutron fields with peak energies of 5.00 MeV and 15.10 MeV in open geometry in the low-scattering experiment hall. At both facilities the detector was placed with its long axis parallel to the incident neutrons, with a target-detector separation of 2.5 m (n-lab) and 1.7 m (AMANDE) to the centre of the detector.

Measurements were also made at the fast neutron facility (Mosconi et al., 2010) at iThemba Laboratory for Accelerator-Based Sciences (iTL), South Africa, using a neutron field produced via the ^{7}Li(p, n)^{7}Be reaction by irradiating a ^{nat}Li target of thickness 8.0 mm with a proton beam of energy 66.0 MeV from the k = 200 separated sector cyclotron. A 2.0 m thick steel and wax wall has two square collimating apertures of inner dimensions 4.5 cm × 4.5 cm which allow for measurements

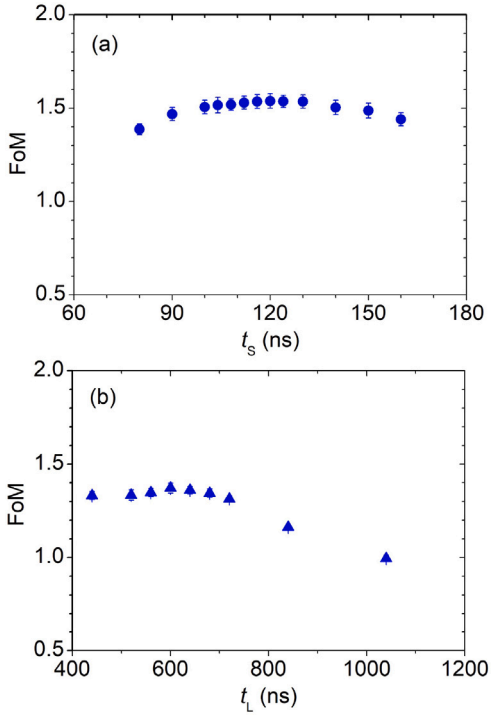

Fig. 6. Figure-of-Merit (FoM) as a function of: (a) short integration time t_S for a fixed long integration time t_L = 840 ns; and (b) long integration time t_L for a fixed short integration time t_S = 120 ns.

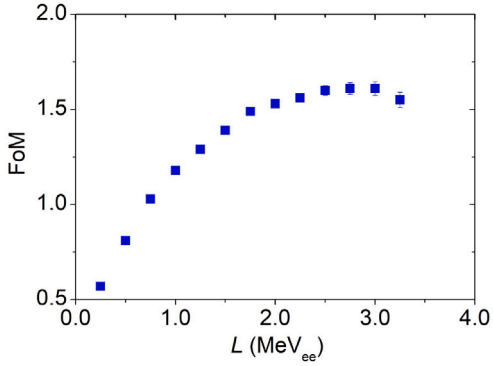

Fig. 7. Figure-of-Merit (FoM) as a function of light output parameter L for the data measured with the AmBe source (Fig. 4).

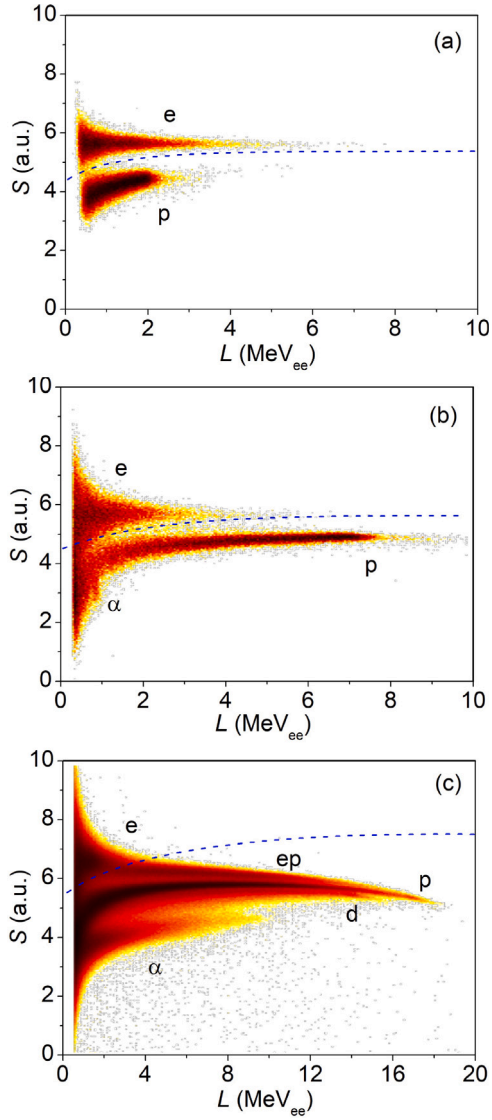

Fig. 8. Event density, shown on a logarithmic colour scale, of the pulse shape parameter S as a function of light output parameter L for neutrons and gamma rays from: (a) a 1.84 MeV deuteron beam irradiating a 793 μg cm^{-2} TiD target (AMANDE), producing neutrons of peak energy 5.00 MeV; (b) the D-T STNG producing 14.1 MeV neutrons (n-lab); and (c) a 66.0 MeV proton beam irradiating a ^{nat}Li target of thickness 8.0 mm, producing neutrons in the range 5.0 MeV to 64.0 MeV (iTL), individually normalised by the total number of measured events. The labels indicate event distributions associated with recoiling electrons (e) protons (p), deuterons (d), tritons (t), and alpha particles (α), and protons which escape from the detector (ep) before depositing all of their energy.

at 0° and 16° relative to the direction of the proton beam. In the present work measurements were made at 8.04 m at 16° to the target. A beam pulse selector can suppress a chosen fraction of proton bunches to enlarge the time interval between pulses, which allows time-of-flight (TOF) measurements to be carried out. For measurements with 66.0 MeV proton beams the time between pulse selector reference pulses is 305 ns with an intrinsic timing resolution of about 1 ns.

Normalised event density plots of the pulse shape parameter S as a function of light output parameter L are shown in Fig. 8 for neutrons and gamma rays from: (a) a 1.84 MeV deuteron beam irradiating a 793 μg cm^{-2} TiD target (AMANDE), producing neutrons of peak energy 5.00 MeV; (b) the D-T STNG producing 14.1 MeV neutrons (n-lab); and (c) a 66.0 MeV proton beam irradiating a ^{nat}Li target of thickness 8.0 mm, producing neutrons in the range 5.0 MeV to 64.0 MeV (iTL). Loci are identified which are associated with different charged particles recoiling in the detector, and the dashed lines separate events associated with neutron and gamma ray interactions. In Figs. 8(a) and (b), the separation between the loci associated with recoiling electrons and protons is excellent across the full range of L. In the case of Fig. 8(c), the calculation of a Figure-of-Merit is more complex as it requires the choice of two loci associated with different charged particles (Comrie et al., 2015).

4. Neutron lineshapes and unfolding

Neutron lineshapes, or light output functions for nearly mono-energetic neutrons, were constructed from the neutron time-of-flight measurements undertaken at iThemba LABS. Fig. 9(a) shows a pulse

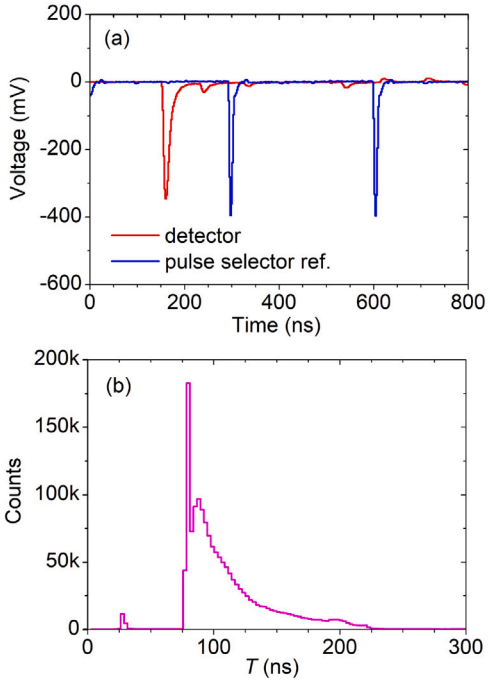

Fig. 9. (a) Typical detector and reference pulse selector pulses used to create the (b) time-of-flight spectrum for neutrons and gamma rays produced by a 66.0 MeV proton beam irradiating an 8.0 mm Li target, measured at 16° to the proton beam.

from a single event in the detector recorded with the pulse selector reference pulses within an 800 ns acquisition window. A time-of-flight parameter T was determined from the time difference between the detector pulse and the first reference pulse after the detector pulse. Fig. 9(b) shows the corresponding time-of-flight spectrum for neutrons and gamma rays produced by a 66.0 MeV proton beam irradiating an 8.0 mm Li target, measured at 16° to the proton beam. The neutron distribution features a 63.5 MeV peak at T = 80 ns associated with the direct ^{7}Li(p,n)^{7}Be knock-out reaction, and a lower energy continuum at longer times associated with breakup reactions (Iwamoto et al., 2011). The small peak feature at T = 30 ns is associated with gamma rays from the target, which were excluded together with the time-independent gamma rays by pulse shape discrimination (Fig. 8(c)).

Fig. 10 shows event density as a function of time-of-flight parameter T and light output parameter L for neutron and gamma rays produced via the ^{7}Li(p,n)^{7}Be reaction, measured at 16° relative to the 66.0 MeV proton beam. After selecting neutron-only events by pulse shape discrimination, nearly mono-energetic neutron lineshapes were then constructed from these data using time-of-flight analyses, and subsequently were used to form the detector response matrix for spectrum unfolding. The response matrix covers a range of neutron energies between 11 MeV and 65 MeV in steps of 3 MeV, and the individual line shapes cover a range of L between 0 and 30 MeV$_{ee}$ in steps of 0.67 MeV$_{ee}$. The ranges and bin widths were chosen based on the limited statistics of the measurement used in the present work to minimise statistical fluctuations in the individual lineshapes.

Fig. 11 shows a selection of the measured lineshapes, each normalised to unity, together with mono-energetic measurements at 5.00 MeV and 15.10 MeV (AMANDE), and 14.1 MeV (n-lab). The measurements made at all three facilities are consistent with each other.

To evaluate the capability of the detector as a neutron spectrometer unfolding analyses were performed using the MAXED program (Reginatto and Goldhagen, 1999; Reginatto et al., 2002), which applies the maximum entropy principle to the problem of spectrum unfolding.

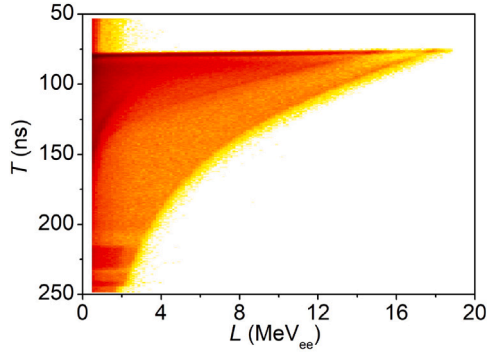

Fig. 10. Neutron event density, shown on a logarithmic colour scale, as a function of light output parameter L and time-of-flight parameter T for measurements made using a 66.0 MeV proton beam irradiating an 8.0 mm Li target, measured at 16° to the proton beam.

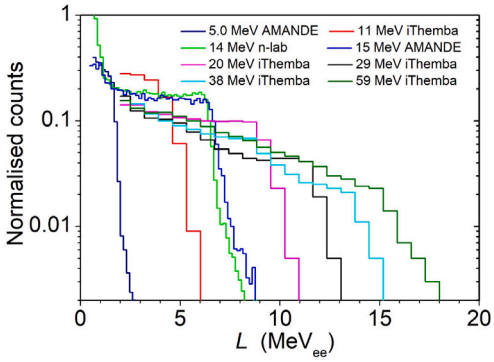

Fig. 11. A selection of quasi-monoenergetic neutron response functions measured via time-of-flight at iThemba LABS together with mono-energetic lineshapes measured at 5.00 MeV and 15.10 MeV (AMANDE) and 14.1 MeV (n-lab), each normalised to unity.

The neutron energy spectrum is deconvolved from the measured light output spectrum, requiring a detector response matrix comprised of mono-energetic neutron light output spectra over the range of interest and an initial estimate of the energy spectrum. The measured detector response matrix was first validated through the unfolding of an artificial "boxcar" spectrum, where a light output spectrum was constructed from the individual lineshapes based on the distribution shown in Fig. 12(a). The artificial light output spectrum was then unfolded with MAXED using a flat spectrum *a priori*, which is considered to be the "worst-case" estimate of the distribution. In all instances the light output spectra were unfolded with lower L limit of 1.0 MeV$_{ee}$, below which the neutron and gamma ray contributions could not be separated. The solution spectrum shown in Fig. 12(b) shows excellent agreement with the original boxcar, with a chi-square value of 1.0 achieved in 720 iterations. Very minor deviations are observed in the 27 MeV to 55 MeV region, which are attributed to the choice of default spectrum, and the similarity of the lineshapes in this region due to the coarse binning structure in L.

The detector response matrix was then used to unfold the light output spectrum measured for neutrons produced via the ^{7}Li(p, n)^{7}Be reaction at 16° relative to the 66.0 MeV proton beam. Fig. 13(a) shows the measured and refolded light output spectra, and the resulting neutron energy spectrum (Fig. 13(b)) is compared to the energy spectrum derived from time-of-flight analyses. Overall, good agreement between the two spectra is observed, with the deviations below 20 MeV attributed to the sensitivity of the unfolding procedure to the lower L threshold used in both the response functions and the measured light output spectrum. As with the boxcar unfolding, some minor deviations in the higher energy regions are observed due to the similarity in the measured response functions in this region.

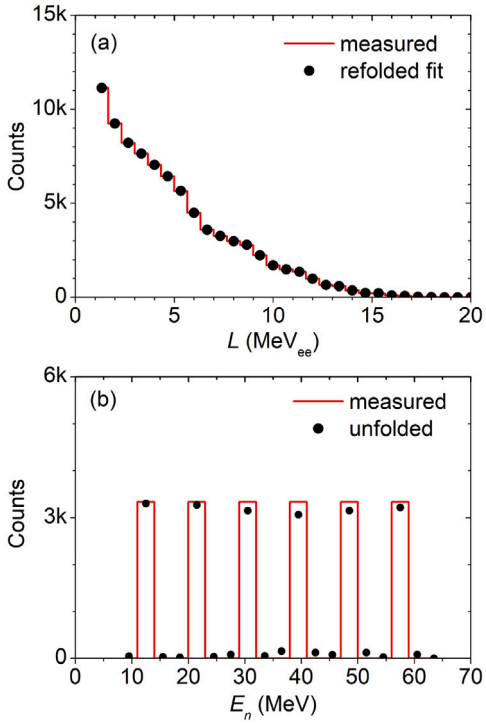

Fig. 12. (a) Artificial light output spectrum L produced using the response functions associated with 14.0 MeV, 23.0 MeV, 32.0 MeV, 41.0 MeV, 50.0 MeV and 59.0 MeV neutrons in equal amounts, together with the refolded light output spectrum from the MAXED analysis. (b) The associated energy spectrum unfolded with MAXED, shown together with the boxcar distribution used to produce the light output spectrum.

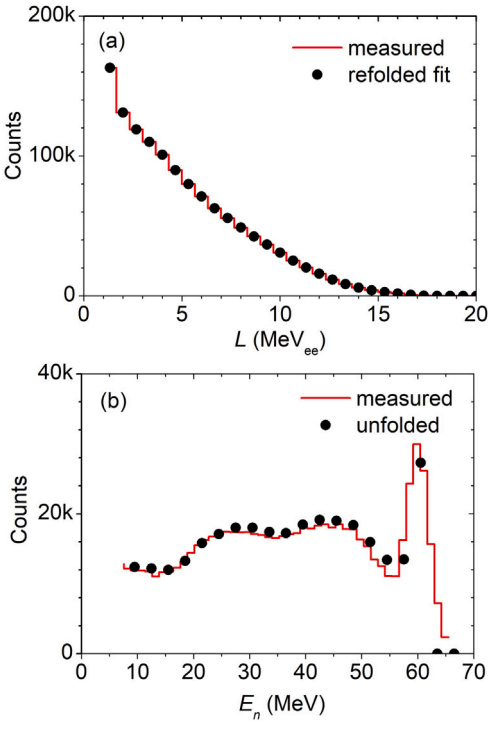

Fig. 13. (a) Light output L spectrum for the neutron field produced by a 66.0 MeV proton beam irradiating an 8.0 mm Li target measured at 16° to the beam together with refolded light output spectrum from the MAXED analysis. (b) The associated energy spectrum unfolded with MAXED shown together with the energy spectrum measured directly from time-of-flight.

5. Discussion and conclusion

A new compact neutron detector system comprised of an EJ-276 plastic scintillator with dimensions 6 mm × 6 mm × 120 mm, single C-series silicon photomultiplier from onsemi (formerly SensL), digital data acquisition and spectrum unfolding was characterised with mono-energetic fast neutron fields with energies between 5.00 MeV and 15.10 MeV at the IRSN AMANDE facility, and the n-lab at the University of Cape Town. As this detector system is being developed for high-energy neutron spectroscopy in aviation and space environments, nearly-monoenergetic response functions were measured between 11 MeV and 65 MeV at the iThemba LABS high-energy neutron facility utilising time-of-flight analyses. Some limitations were noted due to the quality of the edge resolution in the measured light output spectra, and the binning structures utilised in the preparation of the response functions. However, the measured detector response functions were used to unfold energy spectra for neutrons produced via the ^{7}Li(p,n)^{7}Be reaction using a 66.0 MeV proton beam at iThemba LABS, and demonstrated good agreement with the energy spectrum determined from time-of-flight analyses.

Although the present work demonstrates measurements of neutron fields with energies up to 64 MeV, our goal is to construct a spectrometer suitable for measurements up to 200 MeV, well above the enhancement around 100 MeV in the neutron spectrum produced by cosmic rays. It is expected that there will be a non-linear increase in the proportion of charged particles escaping from the detector volume with increasing incident neutron energy, however, the quasi-monoenergetic response functions at higher energies should be sufficiently unique for unfolding analyses due to distinguishing features associated with the n-^{12}C reaction channels (see Fig. 8(c)).

Utilising a single silicon photomultiplier with a long, thin scintillator is known to result in degraded light collection characteristics relative to detectors utilising multiple silicon photomultipliers (Comrie, 2016). However, in this work we have demonstrated that unfolding is still viable as long as the detector response is determined through measurement, and the binning structure chosen accordingly. The present detector strategy was driven by the constraints of compactness and simplicity and it is recognised that improved light collection is achieved using two SiPMs which has been implemented in other detector designs (Buffler et al., 2023). Other future developments include producing a handheld device with a similar form factor and cost as those used for gamma ray detection such as those within the OpenRadiation project (Bottollier-Depois et al., 2019).

CRediT authorship contribution statement

Andy Buffler: Writing – review & editing, Writing – original draft, Visualization, Supervision, Resources, Project administration, Methodology, Investigation, Funding acquisition, Formal analysis, Conceptualization,. **Tanya Hutton:** Writing – review & editing, Visualization, Supervision, Software, Methodology, Investigation, Funding acquisition, Formal analysis, Data curation, Conceptualization. **Erin Jarvie:** Writing – review & editing, Visualization, Software, Methodology, Investigation, Formal analysis. **Richard Babut:** Writing – review & editing, Resources, Project administration, Investigation, Funding acquisition.

Declaration of competing interest

The authors declare that they have no known competing financial interests or personal relationships that could have appeared to influence the work reported in this paper.

Data availability

Data will be made available on request.

Acknowledgements

The authors would like to thank the technical staff of the iThemba LABS and AMANDE facilities for their support in setting up the experiments and for the provision of high quality beams. This work was supported by the National Research Foundation of South Africa (grant ID 138069) and L'Institut de Radioprotection et de Sûreté Nucléaire, France (grant ID 21636).

References

3M ESR, 2023. Enhanced specular reflector film, [online]. https://www.3~m.com/3M/en_US/p/d/b5005047091/.

Bartlett, D., 2004. Radiation protection aspects of the cosmic radiation exposure of aircraft crew. Radiat. Prot. Dosim. 109, 349–355.

Boscolo, D., Scognamiglio, D., Horst, F., et al., 2020. Characterization of the secondary neutron field produced in a thick aluminum shield by 1 GeV/u ^{56}Fe ions using TLD-based ambient dosimeters. Front. Phys. 8:365.

Bottollier-Depois, J., Allain, E., Baumont, G., et al., 2019. The OpenRadiation project: monitoring radioactivity in the environment by and for the citizens. Radioprotection 54, 241–246.

Brenner, D., Hall, E., 2008. Secondary neutrons in clinical proton radiotherapy: A charged issue. Radiother. Oncol. 86, 165–170.

Brooks, F., 1979. Development of organic scintillators. Nucl. Instrum. Methods Phys. Res. 162, 477–505.

Buffler, A., Comrie, A., Hutton, T., 2023. A compact direction-sensitive fast neutron spectrometer. Nucl. Instrum. Methods Phys. Res. A 1052, 168256.

Buffler, A., Comrie, A., Smit, F., Wörtche, H., 2015. Neutron spectrometry with EJ299-33 plastic scintillator for E_n = 1 - 100MeV. IEEE Trans. Nucl. Sci. 62, 1422–1428.

Buffler, A., Comrie, A., Smit, F., Wörtche, H., 2016. A new compact neutron/gamma ray scintillation detector. Internat. J. Modern Phys. 44, 1660228.

CAEN, 2023. DT5730 digitizer, [online]. https://www.caen.it/products/dt5730/.

Cecconello, M., 2019. Liquid scintillators neutron response function: a tutorial. J. Fus. Energy 38, 356–375.

Comrie, A., 2016. A New Compact Neutron Spectrometer (Ph.D. thesis). University of Cape Town, https://open.uct.ac.za/handle/11427/36908.

Comrie, A., 2023. QtDAQ, [online]. https://github.com/veggiesaurus/qtdaq.

Comrie, A., Buffler, A., Smit, F., Wörtche, H., 2015. Digital neutron/gamma discrimination with an organic scintillator at energies between 1 MeV and 100 MeV. Nucl. Instrum. Methods Phys. Res. A 772, 43–49.

Dietze, G., Klein, H., 1982. NRESP4 and NEFF4 - Monte Carlo Codes for the calculation of the neutron response functions and detection efficiencies for NE 213 scintillation detectors, PTB-ND-22. Technical report, PTB Braunschweig.

Eljen Technology, 2023. EJ-276 plastic scintillator, [online]. https://eljentechnology.com/products/plastic-scintillators/ej-276.

Goldhagen, P., Clem, J., Wilson, J., 2004. The energy spectrum of cosmic-ray induced neutrons measured on an airplane over a wide range of altitude and latitude. Radiat. Prot. Dosim. 110, 387–392.

Gressier, V., Bonaldi, A., Dewey, M., et al., 2014. International key comparison of neutron fluence measurements in monoenergetic neutron fields: CCRI(III)-K11. Metrologia 51, 06009.

Gressier, V., Guerre-Chaley, J., Lacoste, V., et al., 2004. AMANDE: a new facility for monoenergetic neutron fields production between 2 keV and 20 MeV. Radiat. Prot. Dosim. 110, 49–52.

Heilbronn, L., Borak, T., Townsend, L., et al., 2015. Neutron yields and effective doses produced by galactic cosmic ray interactions in shielded environments in space. Life Sci. Space Res. 7, 90–99.

Hutton, T., Buffler, A., 2024. Characterisation of neutron fields at the n-lab, a fast neutron facility at the University of Cape Town. Appl. Rad. Iso. 111196.

Iwamoto, Y., Hagiwara, M., Satoh, D., et al., 2011. Quasi-monoenergetic neutron energy spectra for 246 and 389 MeV ^{7}Li(p,n) reactions at angles from 0° to 30°. Nucl. Instrum. Methods Phys. Res. A 629, 43–49.

Mosconi, M., Musonza, E., Buffler, A., et al., 2010. Characterisation of the high-energy neutron beam at iThemba LABS. Radiat. Meas. 45, 1342–1345.

Ngo, K., Cazzaniga, C., Paoletti, M., et al., 2023. Fast neutron response characterization of an EJ-276 plastic scintillator for use as a neutron monitor. Nucl. Instrum. Methods Phys. Res. A 1051, 168216.

Nolte, R., Thomas, D., 2011. Monoenergetic fast neutron reference fields: II. Field characterization. Metrologia 48, S274–S291.

onsemi, 2023. C-series silicon photomultiplier, [online]. https://www.onsemi.com/pdf/datasheet/microc-series-d.pdf.

Reginatto, M., Goldhagen, P., 1999. MAXED, a computer code for maximum entropy deconvolution of multisphere neutron spectrometer data. Health Phys. 77, 579–583.

Reginatto, M., Goldhagen, P., Neumann, S., 2002. Spectrum unfolding, sensitivity analysis and propagation of uncertainties with the maximum entropy deconvolution code MAXED. Nucl. Instrum. Methods Phys. Res. A 476, 242–246.

Ryabeva, E., Urupa, I., Lupar, E., et al., 2021. Calibration of EJ-276 plastic scintillator for neutron–gamma pulse shape discrimination experiments. Nucl. Instrum. Methods Phys. Res. A 1010, 165495.

Sole, C., Buffler, A., Hutton, T., et al., 2022. Benchmarking a new digital data acquisition system for fast neutron metrology. IEEE Trans. Nucl. Sci. 69, 1780–1788.

Zaitseva, N., Glenn, A., Mabe, A., et al., 2018. Recent developments in plastic scintillators with pulse shape discrimination. Nucl. Instrum. Methods Phys. Res. A 889, 97–104.

Zeitlin, C., Castro, A., Beard, K., et al., 2023. Results from the Radiation Assessment Detector on the International Space Station, Part 2: The fast neutron detector. Life Sci. Space Res. 39, 76–85.